PARTICLE DETECTOR FOR LOW ENERGY HEAVY IONS

An Undergraduate Research Scholars Thesis

by

KARTHIK RAO

Submitted to the Undergraduate Research Scholars Program at
Texas A&M University
in partial fulfillment of the requirements for the designation as an

UNDERGRADUATE RESEARCH SCHOLAR

Approved by Research Advisor: Dr. Grigory Rogachev

May 2020

Majors: Physics
Computer Science

TABLE OF CONTENTS

ABSTRACT

Particle Detector For Low Energy Heavy Ions

Karthik Rao
Department of Physics and Astronomy
Department of Computer Science and Engineering
Texas A&M University

Research Advisor: Dr. Grigory Rogachev
Department of Physics and Astronomy
Texas A&M University

The purpose of this research is to build, calibrate and test a parallel-plate avalanche counter (PPAC) detector, which can be used to detect low energy heavy ion particles. This detector will enable Texas A&M to conduct experiments using low energy heavy ions with the MDM magnetic spectrometer, which was not possible previously. It will be used primarily in experiments in nuclear astrophysics that utilize indirect methods such as the sub-Coulomb transfer reaction and the Trojan Horse method. The expected outcomes are that the detector can separate particles with equal magnetic rigidities, but different mass/charge ratios. It should be able to measure the time of flight for particles as they move from one end of the detector to the other. It should also be able to locate, with sufficient precision, the coordinates of the particle inside the detector so that the actual path which a particle takes can be found.

DEDICATION

To my parents who have always believed in me, and without whose support, I couldn't have achieved this

ACKNOWLEDGMENTS

I would like to express my heartfelt gratitude to my advisor Dr. Grigory Rogachev for giving me this invaluable opportunity to work with him. Without his remarkable knowledge and infectious enthusiasm, this work would have been extremely difficult.

I would also like to thank Dr. Heshani Jayatissa, who started work on this project and whose support and mentorship proved invaluable to my efforts.

I am also indebted to Dr. Greg Chubaryan for all his support through each step this project. This work would not have been possible without him.

Additional thanks goes to Emily Harris, Dr. Yevgen Koshchiy, Sunghoon (Tony) Ahn for their invaluable help with this experiment.

Finally, I would like to thank the Cyclotron Institute support staff, the Cyclotron Operations Group, and the machine shop staff, for their help and assistance with the work behind this project

The project is funded by the U.S. Department of Energy, Office of Science, Office of Nuclear Science, under Award No. DE-FG02-93ER40773.

NOMENCLATURE

TAMU	Texas A&M University
PPAC	Parallel-Plate Avalanche Counter
P	Pressure
T	Time
TOF	Time Of Flight
THM	Trojan Horse Method
ANC	Asymptotic Normalization Coefficient
CD	Coulomb dissociation
CFD	Constant Fraction Discriminator
TAC	Time to Amplitude Converter
ADC	Analog to Digital Converter
DAQ	Data Acquisition

LIST OF FIGURES

FIGURE Page

LIST OF TABLES

TABLE Page

CHAPTER I

INTRODUCTION

Purpose

Understanding the origin of elements in the universe is a fundamental question that has presented several challenges, both theoretically and experimentally. As discussed in "The Origin of Chemical Elements"[2], it was originally thought that all the chemical elements in the Universe were created in the Big Bang Explosion by neutron capture reactions brought about by the rapid expansion and cooling of primordial matter. This paper argued that the protons, subatomic particles with a positive charge, led to the formation of deuterium nuclei, which are heavier hydrogen nuclei. The nuclei collided to neutrons and merged with them, which led to the creation of heavier chemical elements. While this theory accounted for the large abundances of hydrogen and helium in the Universe, it was later demonstrated that elements with atomic numbers greater than 3 could not be efficiently produced in the Big Bang.

Due to this, another theory was proposed by Burbidge, Burbidge, Fowler and Hoyle in their "B^2FH"[3] paper. This paper proposed that most of the chemical elements found in the Universe were created in the interior of stars. While hydrogen, helium and lithium were formed as a result of the Big Bang, the other elements were created due to nucleosynthesis processes that occurred in stellar environments. This work laid the foundation for modern understanding of the origin of chemical elements. Elucidating chemical evolution of the universe constitutes a major part of nuclear astrophysics[4].

Nuclear reactions with charged particles play a major role in nucleosynthesis. Most of these reactions occur in cycles in which hydrogen burns[5]. One example of such a reaction is the Carbon-Nitrogen-Oxygen cycle, which occurs once carbon is produced in stars. This reaction produces more energy compared to the first stage of hydrogen burning reactions. This increased energy heats up the star and leads to more nuclear reactions which results in the formation of new

nuclei. Unfortunately, the conditions under which these reactions occur makes it difficult to study directly the rate of these reactions in laboratory conditions. For instance, these reactions occur at energies well below the Coulomb barrier, which makes their cross section too small to measure [4].

The Coulomb barrier is the energy barrier due to electrostatic interaction between two nuclei. This barrier must be overcome before the nuclei can get close enough to interact. Since the reactions occur at sub-Coulomb energies in stars, but are measured at energies much higher in laboratories, significant uncertainty is present in the measurements. To overcome this, indirect methods have been developed to measure the information about these reactions which allow us to determine their rate.

Primarily, there are two types of measurements in nuclear physics for astrophysics; Direct and Indirect measurements [6]. Direct measurements are done when reactions are reproduced in laboratories at the energies at which they occur in stars. However, these energies are below the Coulomb barrier which leads to small cross-sections, making measurements difficult. The signal-to-background noise is small and this increases the uncertainty of measurements. Measures have to be taken to increase the accuracy, which include extrapolating the data down to energies in the Gamow Window. The Gamow window is the probability factor of two of two nuclear particles overcoming the Coulomb barrier and undergoing nuclear reactions [7].

The other type of measurements are indirect measurements in which beams at labs are used to extract data from which cross-sections at energies relevant to processes occurring in stars are evaluated. This also helps when the reactions involve unstable radioactive nuclei. There are several different common indirect techniques, such as the Asymptotic Normalization Coefficient method, Trojan Horse method and Coulomb dissociation method [8].

The Trojan Horse Method (THM) allows us to determine the reaction rate for reactions by obtaining the cross section for a process using a surrogate "Trojan Horse" particle [9]. Since the process using the surrogate particle occurs at energies above the Coulomb barrier, the reaction's cross section can be determined with higher accuracy. The Coulomb dissociation (CD) method

uses the virtual photon flux from the interaction of a high-energy ion with a very heavy target to dissociate the heavy ion and is mostly suited when targets are not stable radioactively [10]. Direct capture reactions of astrophysical interest often involve systems where the binding energy of the captured particles is low. The capture occurs through the tail of the nuclear overlap function in the corresponding two-body channel [4]. The normalization of this tail, which is based on the quantum overlap of bound state wave functions of the initial and final nuclei involved in the reactions [11, 8]. All of these indirect methods provide information about the reactions occurring in stars at energies that can be measured in labs without high uncertainty.

Experimental Challenges

Currently, the Cyclotron is equipped with particle detectors and spectrometers which allow us to conduct experiments using these indirect methods. However, the current detector is not capable of being used in experiments with particular low-energy heavy ions such as ^{16}O ions due to the 25 μm thick Kapton entrance window of the Oxford detector located after the spectrometer since these ions will not be able to penetrate the detector to be measured. Therefore, a new focal plane particle detector has to be built which allows us to study reactions using these low-energy heavy ions. The main goal of this project is to build and characterize a high position resolution and high timing resolution detector that can be used in the focal plane of the MDM spectrometer for detection and identification of heavy ions with energies of approximately 1 MeV per nucleon.

CHAPTER II

METHODS

Operation of a PPAC detection

A PPAC detector is a proportional counter detector where electron amplification occurs in two very uniform fields. This detector contains two parallel planar electrodes (cathodes) on either side of a common electrode (anode). The two cathodes are composed of a uniform grid of wires made of 50 μm Be-Cu alloy with a pitch of 1 mm. The two cathodes are different based on the orientation of the wires in them. One of the cathodes has wires placed vertically and this plane is labelled the X-plane. The other cathode has the wires placed horizontally and this plane is called the Y-plane. The cathode consists of a thin mylar foil of thickness 220 μg/cm^2 with an aluminum layer of thickness 80 μg/cm^2 on either side of the mylar foil. The anodes and cathode have a separation of approximately 3 mm. This separation is created by the printed circuit board which is used to hold the wires and the foil. Figure 1 shows a typical schematic of PPAC detectors.

Typically, the detector has an entrance and exit window in order to contain a gas volume for electron amplification. In this case, both the PPAC detectors are placed in one large gas volume which removes the need for separate entrance and exit window foils for each detector. This is optimal since having separate entrance and exit windows for the two detectors can further reduce the energy of a particle travelling through the detectors, making measurements impossible for the lowest energy particles. The gas used for the detector is pentane (C_5H_{12}) with a pressure of approximately 6 Torr.

A particle travelling though a PPAC detector will ionize the gas between the cathodes and anode creating electron-ion pairs. These electrons and ions will travel through the uniform electric field towards their respective electrodes. The electrons will create a *Townsend avalanche* and create many similar electron-ion pairs. A Townsend avalanche is a gas ionization process where free electrons are accelerated by an electric field, collide with gas molecules and free additional

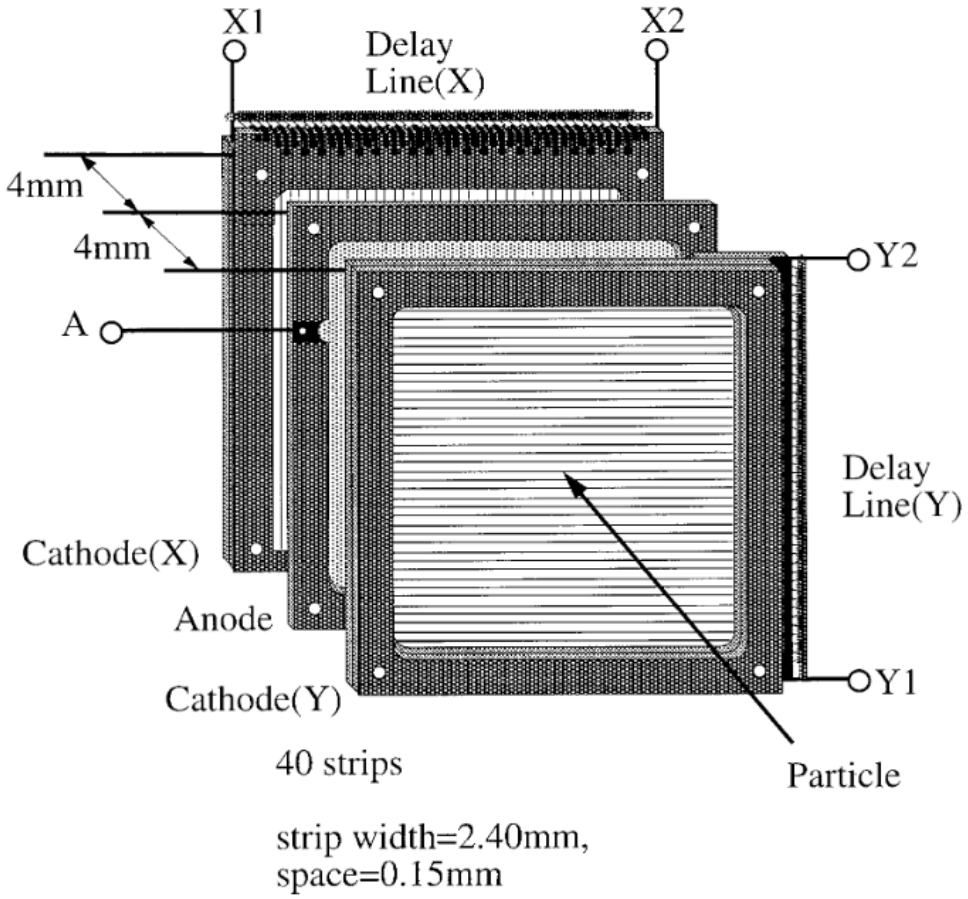

Figure 1: Typical schematic of a 100×100 mm^2 active area PPAC detector [1].

electrons as a result. This process repeats itself and the freed electrons are accelerated and free additional electrons. This results in an avalanche multiplication that permits electrical conduction through the gas which is normally insulating.

The total charge from the electrons will then be collected by the individual cathode wires and produce a signal. These detectors operate on the proportional region of the gas where the total amount of charge collected at the electrodes are proportional to the number of electron-ion pairs created by the initial particle. The number of primary electrons produced by the initial particle of interest is proportional to the rate of increase in the number of electrons, as shown in the equation

below.

$$\frac{dN}{dz} = \alpha N \tag{Eq. 1}$$

where N, z, α represents the number of electrons created, the traveled distance along the electrode gap (from the point of primary ionization to the electrode) and the first Townsend coefficient (which depends on the electric field and the pressure of the gas used) respectively. In an uniform electric field such as the one used in this detector, α is constant but depends on the reduced electric field, S. The relation between Townsend coefficient and reduced electric field is as follows,

$$\frac{\alpha}{p} = K \cdot S^m \cdot \exp^{\frac{-L}{S^{1-m}}} \tag{Eq. 2}$$

where K, L, m are constants related to the gas, with the value of m [12] ranging from 0 to 1, and p is the pressure of the gas.

$$N = N_0 \cdot \exp^{\alpha z} \tag{Eq. 3}$$

By substituting $N = N_0$ in equation Eq. 1, where N_0 is the number of initially ionized electrons, the Townsend avalanche equation can be obtained as seen in equation Eq. 3. This equation holds only if the initial electrons were formed from a single point. Since primary electrons are formed uniformly along the trajectory of the charged particle as it goes through the detector, the equation has to be modified. As the particle travels through the electrode gap of size D, the number of electrons formed is given by Eq. 4.

$$N = \int_0^D \frac{N_0}{D} . e^{\alpha z} dz = \frac{N_0}{\alpha D}(e^{\alpha D} - 1) \tag{Eq. 4}$$

Since $e^{\alpha D} >> 1$, Eq. 4. can be approximated to give Eq. 5.

$$N = \frac{N_0}{\alpha D} . e^{\alpha D} \tag{Eq. 5}$$

When z is equal to D, the limit tends to Eq. 6.

$$N_0 \rightarrow \frac{N_0}{\alpha D} \qquad \text{(Eq. 6)}$$

This shows that the number of primary electrons are multiplied by a factor of $\frac{1}{\alpha D}$, that is, the number of effective primary electrons is $\frac{1}{\alpha D}$ times the number of electrons that are initially formed between the electrodes.

Design and Manufacture of a PPAC detector

A PPAC detector consists of 3 electrodes: one anode between two cathodes separated by a distance of 3 mm on either side. The detector has an active area of 40 cm x 10 cm. These electrodes are displayed in Figures 2 to 6.

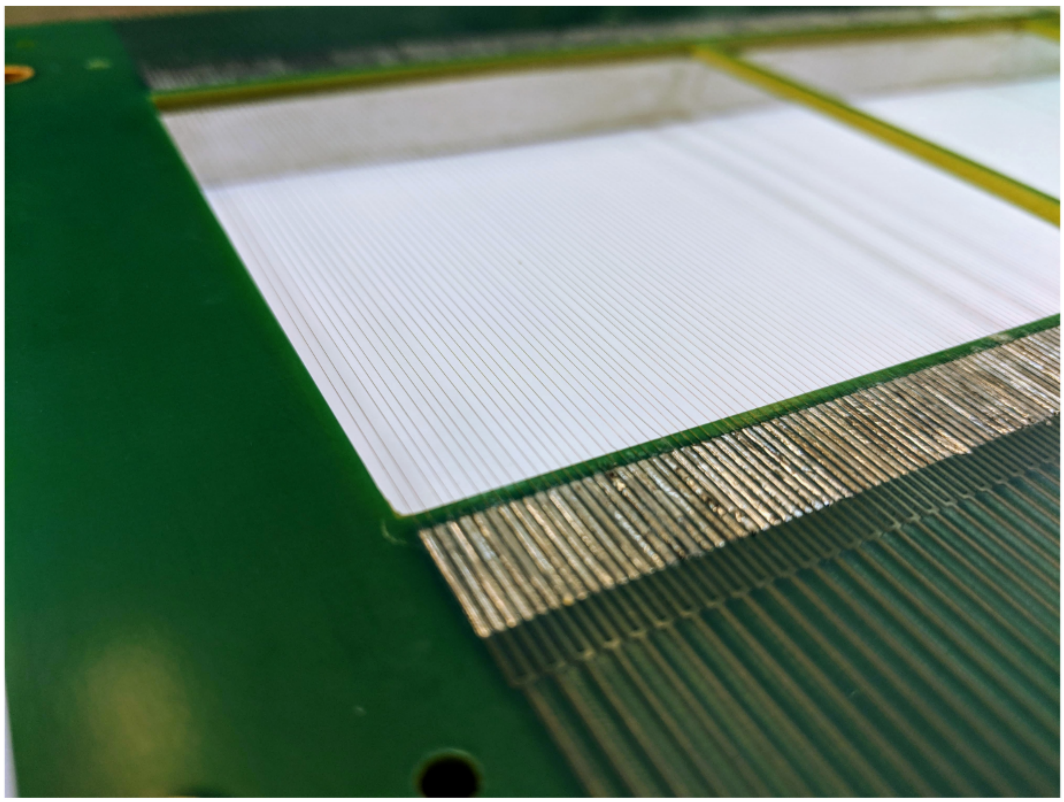

Figure 2: A picture of the Be-Cu wires soldered on to the pads of the X-direction cathode of the PPAC detector.

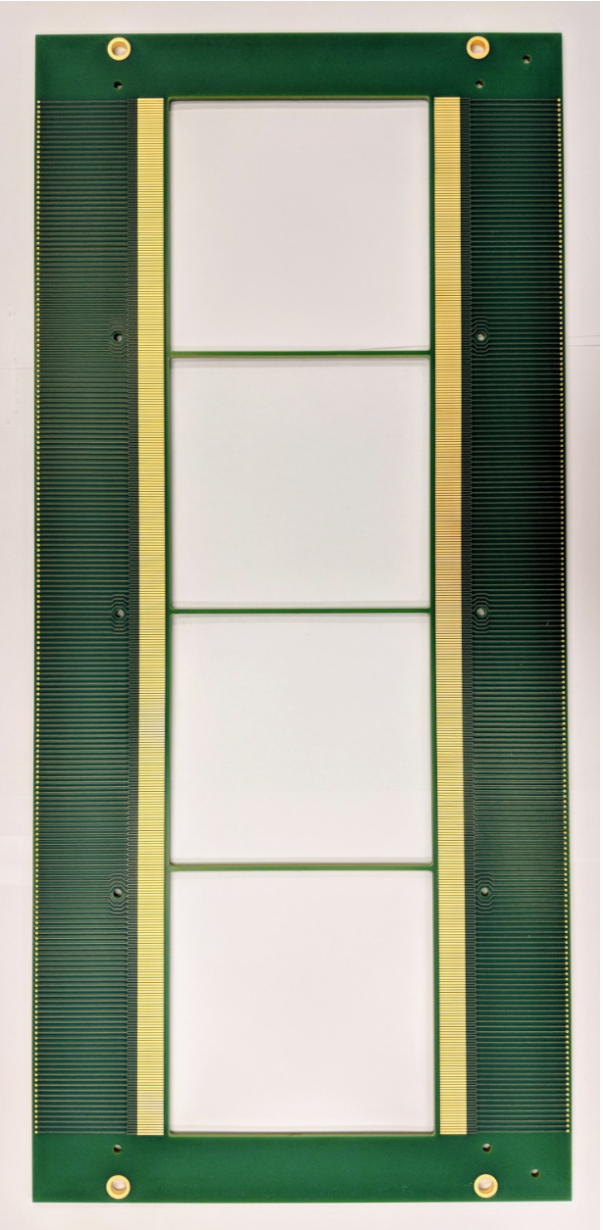

Figure 3: Front view of the bare X-plane cathode of the PPAC detector before connecting the Be-Cu wires.

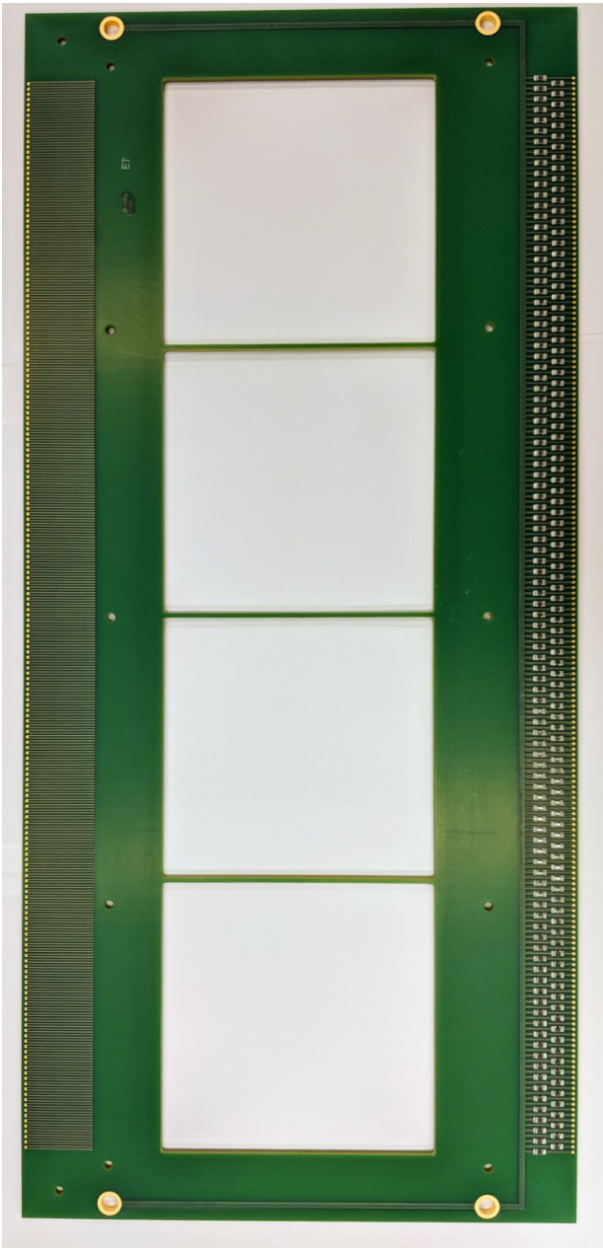

Figure 4: Back view of the bare X-plane cathode of the PPAC detector before connecting the Be-Cu wires.

Figure 5: Front view of the bare Y-plane cathode of the PPAC detector before connecting the Be-Cu wires

Figure 6: Back view of the bare Y-plane cathode of the PPAC detector before connecting the Be-Cu wires

The PCBs have a thickness of 0.125 inches (3 mm) and a copper weight of 2 oz, covered by a plating of immersion gold to ensure an extremely uniform surface flatness. The cathodes consists of an equally-spaced array of fine wires to give the position of a charged particle travelling through the active region. The wire used for this detector is a Be-Cu alloy of 50 μm diameter and the pitch between each wire is 1 mm. A picture of a cathode after soldering these wires are shown in Figure 2. These wires are soldered on to individual the gold-plated pads that can be seen on the front views of the X and Y cathodes.

At one end of these soldered wires, each two wires are combined together and connected to a surface-mounted resistor of 910 kΩ, which are all connected to a common ground on one side. The array of these surface-mounted resistors can be seen in Figures 4 and 6. The other end of the individual wire signals are carried to the back side of the cathode plates and read using resistive delay lines.

For the two X and Y direction cathode boards, three 1 mm wide strips of the printed circuit board were left in the active area at 10 cm intervals along the horizontal direction for rough calibration purposes as well as support for the wires. Specially for the Y-direction cathode, the 40 cm long wires could sag in the electric field without such a support.

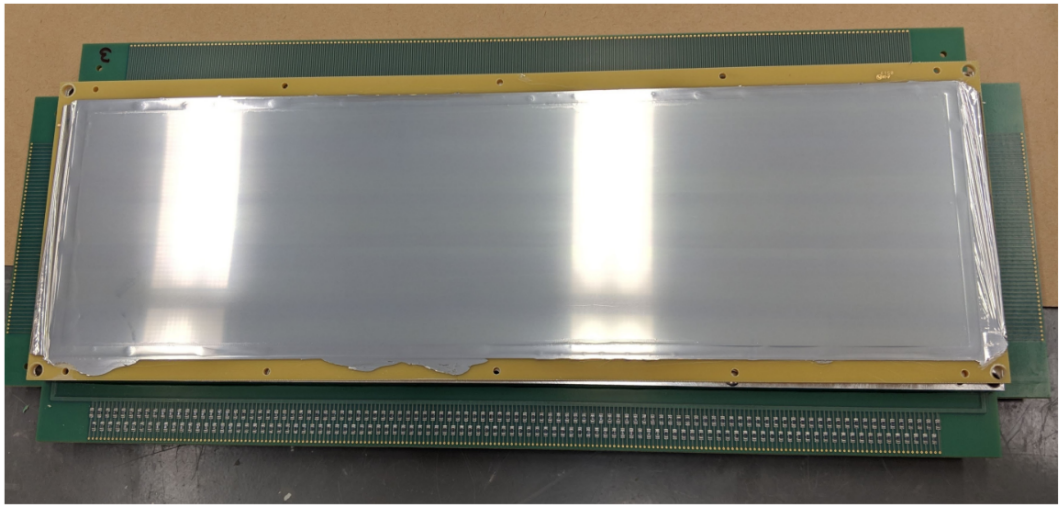

Figure 7: A picture of the PPAC anode foil glued on to the PCB frame.

Figure 7 displays the anode with the foil glued on to the frame. The anode consists of a double-sided mylar foil stretched and glued on a PCB frame. The mylar foil has a thickness of 220 μg/cm^2 (1 μm), and is coated on either side with a layer of aluminum (80 μg/cm^2). Both sides of the mylar foil should be supplied the same voltage simultaneously. This is done by folding the foil on to itself along one edge, and then biasing one side of the foil. It is extremely important to ensure that this mylar foil has no ripples after gluing to the PCB frame. Any ripples present will compromise the uniformity of the electric field along the active region. It is also important to ensure the foil does not have any holes in it. These holes also affect the uniformity of the electric field.

The delay line is prepared by wounding a coated copper (Cu) wire around a PCB. The pitch of the wire on the delay line is related to the diameter of the wire according to the equation below. The main reason for needing a delay line is to simplify data acquisition. After an avalanche multiplication as described in the previous sub-section occurs, a current is induced in the cathode wires closest to where the avalanche occurred. The induced signal in the cathode wires build up two waves in the delay line in opposite direction. These travelling waves are the result of the sum of contributions of induced signals from the cathode. By using the anode signal as a common start and measuring the time delays for the integrated waves to reach the amplifiers at each end of the delay line, the impact point (where ionising took place) can be determined with high accuracy. [13]

Using electronics such as CFDs and TACs, the position of where the ionising occurred can be calculated. The anode signal serves as the common start signal. The waves in the delay line in each direction give an ending signal, whose time can be denoted by T_l for signal in the left direction, and T_r for signal in the right direction. By calibrating the electronics, the offset (a) and slope (b) can be determined. Using this information and equations Eq. 8 and Eq. 9, the absolute x-position (x) and absolute y-position (y) of the incident particle can be calculated. The process of

calibration and electronics used are described in the next sub-section.

$$\frac{\text{Distance between wires (pitch)}}{\text{Diameter of the wire}} = 2.27 \qquad \text{(Eq. 7)}$$

$$x = (T_r - T_l) \times b + a \qquad \text{(Eq. 8)}$$

$$y = (T_r - T_l) \times b + a \qquad \text{(Eq. 9)}$$

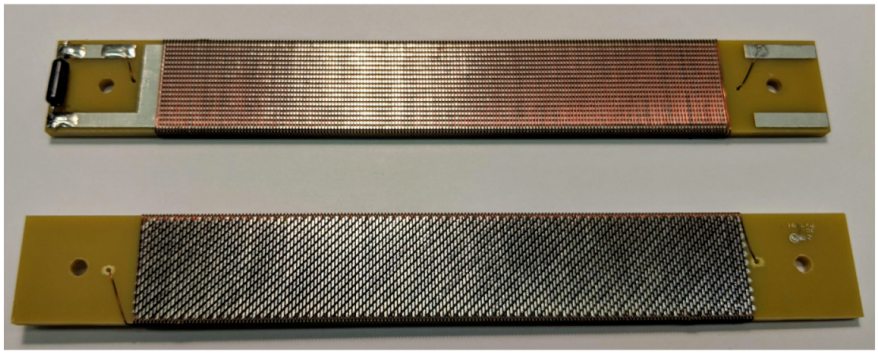

Figure 8: A picture of the front (top) and back (bottom) views of a delay line.

The copper wire used for the delay lines of this PPAC detector has a diameter of 0.011 inches (0.2794 mm). Using Eq. 7, the pitch is found to be 0.025 inches. A Figure of a delay line used for this PPAC detector is shown in Figure 8. This delay line has a 287 Ω impedance. The effective length of the delay lines are 40 cm and 10 cm for the X and Y cathodes, respectively.

Once the electrodes and the delay lines are prepared, they are assembled to complete a PPAC detector (Figure 9). A picture of the ordering of the individual components of the detector is shown in Figure 10. A blank spacer board (*D* in Figure 10) made of the same PCB thickness as the anode board is used to create the 3 mm gap between the anode and the X-cathode. A groove is carved out on the side of the spacer to accommodate the thickness of the teflon-coated wire soldered to the anode board to provide the bias for the anode. All the components are held together

using metal screws which are surrounded by heat shrink tubing to avoid any electrical connections between the electrodes. Once fully-assembled, a 1500 V bias in air was applied to the anode foil and the ground was connected to aluminum frames holding the cathodes to check for unwanted electrical connections.

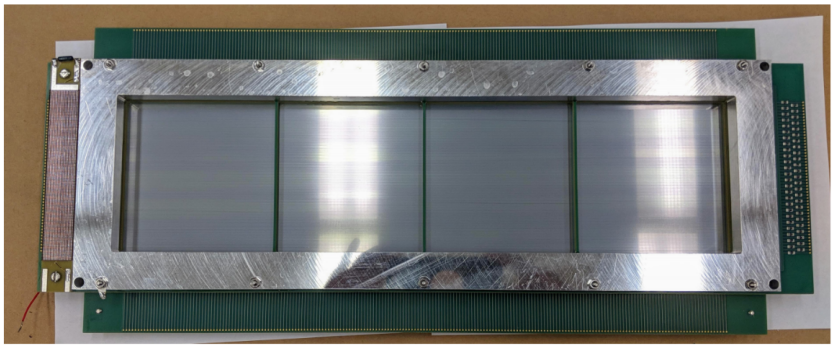

Figure 9: Top view of a fully assembled PPAC detector.

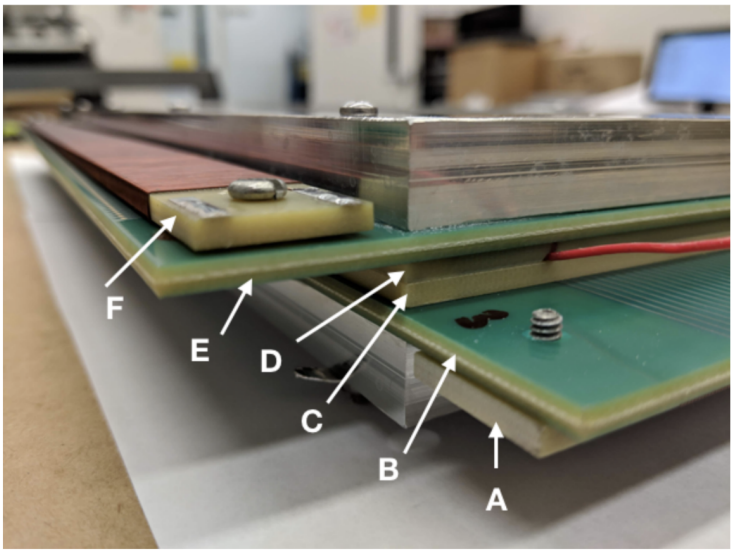

Figure 10: A picture of the order of the individual components of a PPAC detector. A) Delay line for Y-cathode B) Y-cathode C) PCB with mylar foil glued on the top D) Spacer E) X-cathode F) Delay line for X-cathode.

After assembling the detectors, two detectors are placed in the large cuboidal steel box pictured in Figure 11. Both the detectors have a gap of 40 cm between them. After carefully placing the detectors as shown in Figure 12, the entire box is sealed and vacuumed to 0 atm using a vacuum pump. Then, the mixture of nitrogen and pentane gas is allowed to flow inside until the pressure reaches 6 torr.

Testing the PPAC detector

After building and assembling the detectors, it is tested to determine it's accuracy. The testing process involves using the electronics displayed in Figure 13. The detectors were tested using an α source of ^{241}Am.

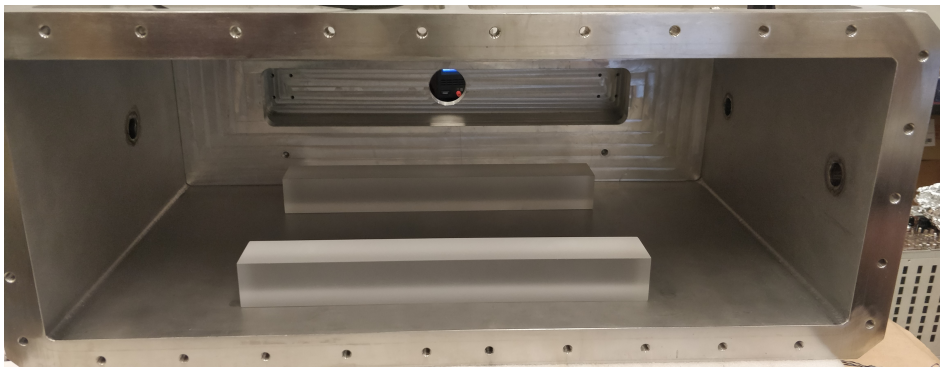

Figure 11: Cuboidal Steel Box to contain the two sets of detectors

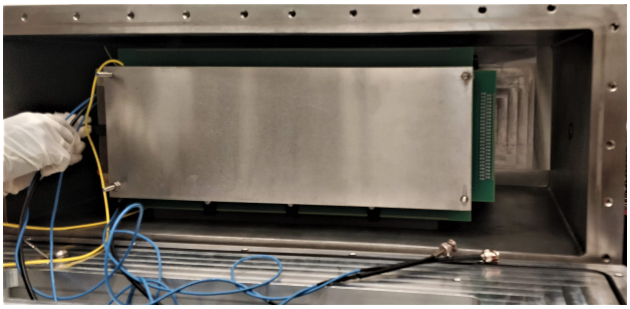

Figure 12: Two sets of detectors inside the steel box for testing

The electric signals generated by the two PPACs are sent to pre-amplifiers using the connector showed in Figure 14. The pre-amplifiers convert weak input electric signals to output signals that are noise tolerant. This signal is sent to fast timing amplifiers which boosts the linear signals without any modification to the shape. These signals are then processed by a Constant Fraction Discriminator (CFD) which finds the maximum of the pulses and generates output signals with a fast rising edge. These are then sent to Time to Amplitude Converters (TAC) which convert time intervals to pulse amplitudes. Since the input signal has a fast rising edge, the time difference is easier to measure and more accurate pulse amplitudes can be generated. Finally, these analog signals are processed by a Analog to Digital Converter (ADC) and digital outputs are displayed by the data acquisition system.

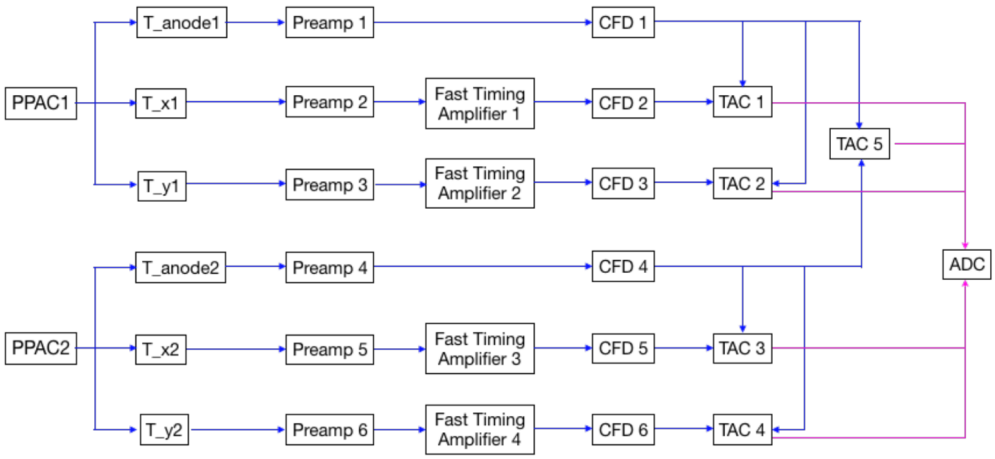

Figure 13: Electronics Scheme used to test the detector

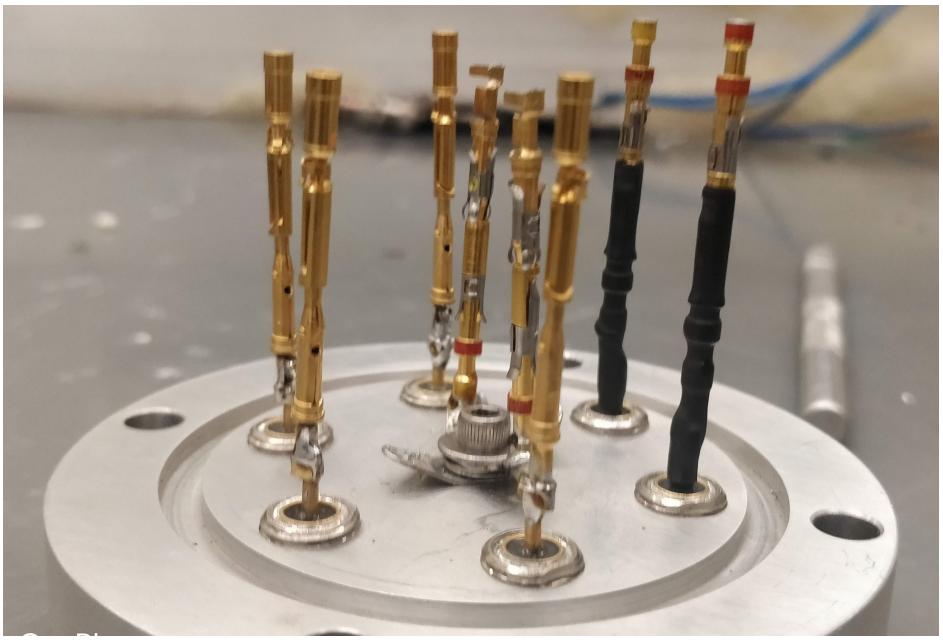

Figure 14: Connector used to connect the internal wires to the external electronics

The code used in the data acquisition system is a modification of the code used in previous experiments to measure data. The code was modified to allow us to input gates on the channels. These gates allow us to localize a small area of measurement in the PPAC and see its effects. For instance, applying gates to X1 and Y1 (a 2d gate), or just X1 (a 1d gate) and seeing what happens with TOF, X2 and Y2, or applying gates just to TOF and checking what is left from X1, X2, Y1, Y2 individually and/or their 2d combinations. To test that the gates were working properly, a signal generator was used that produced signals that were localised around four specific channels. Then, gates were applied to exclude one or more of these channels and results were noted. The histograms from this are displayed in Appendix A (Figures A1 - A3).

After this, the electronics were calibrated to find out the exact ratio between channel number and absolute time under the electronics used. This would allow us to find the exact time for any channel on the spectrum. This was done by measuring the peaks of the signals generated using the signal generator versus the time difference in peaks. These data points were plotted and linearly fitted to find the slope and offset. The data measured and linear fits are displayed in Table A1 and

Figures A4 - A7 in Appendix A. This calibration increases the accuracy of data measured using delay-line readouts.

CHAPTER III

RESULTS

A functioning particle detector was built and assembled and is currently in the process of being tested to find its various properties. Preliminary tests conducted have shown that the detector is successfully able to detect alpha particles using the testing source with an acceptable amount of noise. Figure 15 displays the result of one of these tests, in which alpha particles from test source were allowed to pass through the entire area of detection. The axis correspond to the different channels in which a particle was detected. The source was slowly moved from one end of the detector to the other.

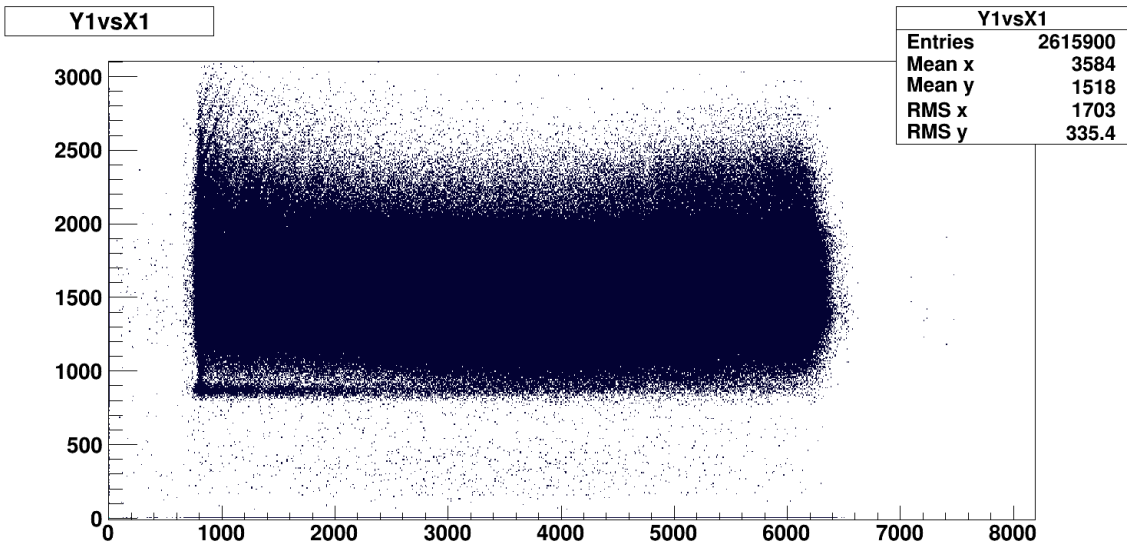

Figure 15: Alpha particle detection results

This test demonstrated that the entire area of detection of the particle detector was capable of detecting particles. Since the area of detection is rectangular, and the particles are not constrained in any direction, it is expected that the graph showing these detection in the XY plane is

rectangular as well. This can be seen in Figure 15, where there is a high concentration of detection in a rectangular area and low concentration outside this area. These are the test results from the detector assembly that was the closest to the source. The X and Y axis represent the channel in which the particle was detected along the x and y directions respectively.

Figure 16 displays the test results when the source was the center and not moved. In this case, we would expect the area near the center of detector to have the most detections and much fewer detections towards the edges of the detector. This is confirmed in the test results. In both these figures, there are detection entries present outside of the expected areas. In Figure 15, there would be no entries present below the 800^{th} channel or above the 3000^{th} channel on the y-axis and to the left of the 1000^{th} channel or the right of the 6600^{th} channel. This is not the case and the biggest reason for this is false detections being made. This may be due to several reasons such as the threshold for deciding whether a signal represents a true detection or not is lower than needed, or there are reflections occurring which lead to multiple detections.

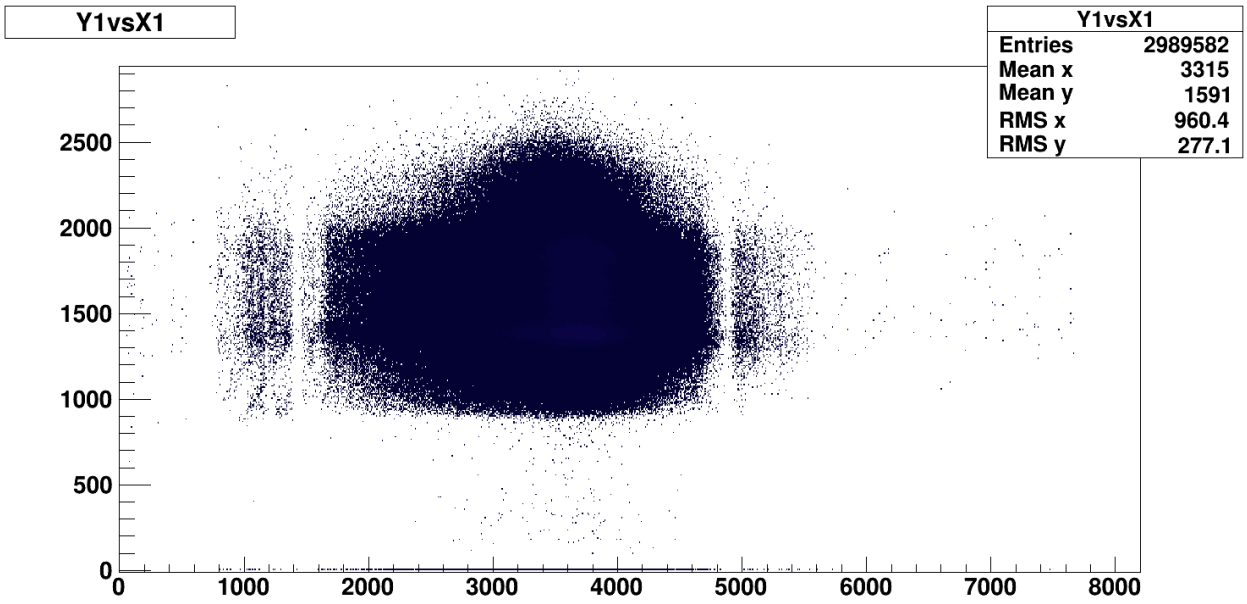

Figure 16: Alpha particle detection results with source at the center and not moved. Notice the strips of detections to the left and right which are caused by false positive detections and reflections

Due to the unforeseen events surrounding the COVID-19 virus in spring 2020, complete data was unavailable at the time of publication for this URS thesis. All graphs produced by testing are present in Appendix A (Figures A8 - A12). Further testing needs to be done to eliminate false detection from noise and blank regions within the rectangular area in Figure 15 indicating no detection. Once testing is complete, the properties of the detector such as energy and time resolution will be determined. After determining these properties, the detector can be used to conduct experiments in nuclear astrophysics involving indirect methods. If the properties determined do not allow for the accuracy and precision required to conduct experiments, parts of the detector such as the foil used in the anode will be replaced with materials that allow us to achieve the accuracy needed. It is expected based on the preliminary tests done so far that the detector is capable of producing results within the needed uncertainty.

CHAPTER IV

CONCLUSION

In this research project, a PPAC particle detector was built and assembled to conduct nuclear astrophysics experiments. Currently, work is still ongoing as the particle detector is being tested to find out its various properties such as timing and energy resolution. The result of these tests will help determine how accurate the detector is and if any changes need to be made in order to improve its accuracy. Once these properties have been determined and found to be within acceptable range of accuracy, the detector will be used in the focal plane of the MDM spectrometer for nuclear astrophysics related experiments that utilize indirect methods. This will allow us to conduct research involving low-energy heavy ions. These experiments will give us further understanding into the origin of elements after the Big Bang.

REFERENCES

[1] H. Kumagai, A. Ozawa, N. Fukuda, K. Sümmerer, and I. Tanihata, "Delay-line ppac for high-energy light ions," *Nuclear Instruments and Methods in Physics Research Section A: Accelerators, Spectrometers, Detectors and Associated Equipment*, vol. 470, no. 3, pp. 562 – 570, 2001.

[2] R. A. Alpher, H. Bethe, and G. Gamow, "The origin of chemical elements," *Phys. Rev.*, vol. 73, pp. 803–804, Apr 1948.

[3] E. M. Burbidge, G. R. Burbidge, W. A. Fowler, and F. Hoyle, "Synthesis of the elements in stars," *Rev. Mod. Phys.*, vol. 29, pp. 547–650, Oct 1957.

[4] R. E. Tribble, C. A. Bertulani, M. L. Cognata, A. M. Mukhamedzhanov, and C. Spitaleri, "Indirect techniques in nuclear astrophysics: a review," *Reports on Progress in Physics*, vol. 77, p. 106901, oct 2014.

[5] C. E. Rolfs and W. S. Rodney, *Cauldrons in the cosmos: nuclear astrophysics*. University of Chicago Press, 2005.

[6] L. Trache and F. Carstoiu, "Indirect methods in nuclear astrophysics," 2019.

[7] J.-H. Yoon and C.-Y. Wong, "Relativistic modification of the gamow factor," *Phys. Rev. C*, vol. 61, p. 044905, Mar 2000.

[8] C. Bertulani, S. Sharma, A. Mukhamedzhanov, A. Kadyrov, A. Kruppa, and D. Pang, "Indirect methods in nuclear astrophysics," *Journal of Physics: Conference Series*, vol. 703, 11 2015.

[9] Tumino, Aurora, Spitaleri, Claudio, Cherubini, Silvio, D´Agata, Giuseppe, Giovanni Luca, Guardo, Gulino, Marisa, Indelicato, Iolanda, La Cognata, Marco, Lamia, Livio, Rosario Gianluca, Pizzone, Giuseppe Gabriele, Rapisarda, Romano, Stefano, Maria Letizia, Sergi, and Spartá, Roberta, "The trojan horse method in nuclear astrophysics," *EPJ Web Conf.*, vol. 184, p. 01016, 2018.

[10] H. Esbensen, "Coulomb dissociation of ^{15}C and radiative neutron capture on ^{14}C," *Phys. Rev. C*, vol. 80, p. 024608, Aug 2009.

[11] L. Trache, "The anc method in nuclear astrophysics," p. 030, 01 2013.

[12] T. Aoyama, "Generalized gas gain formula for proportional counters," *Nuclear Instruments and Methods in Physics Research Section A: Accelerators, Spectrometers, Detectors and Associated Equipment*, vol. 234, no. 1, pp. 125 – 131, 1985.

[13] J. Spanggaard, "Delay wire chambers a users guide," 04 2020.

APPENDIX A

No Gates

No Gates

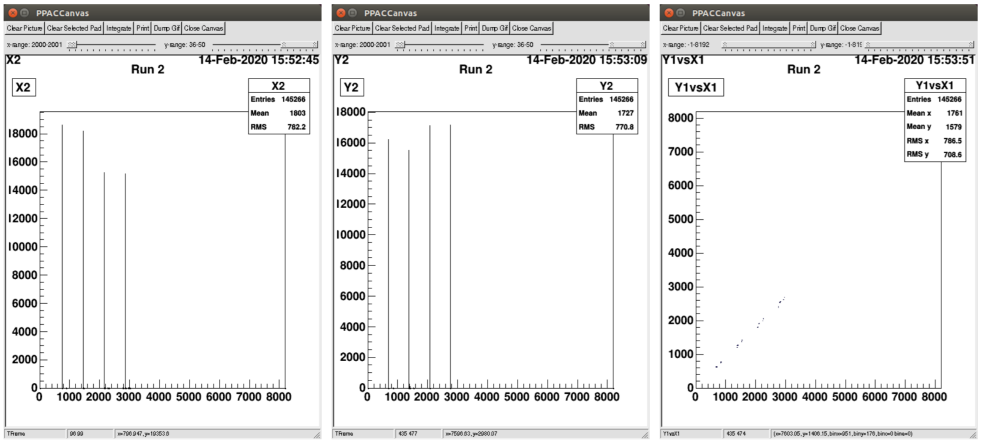

Figure A1: Histogram results with no gates on channels

Gating on X1 (channels 2000-4000)

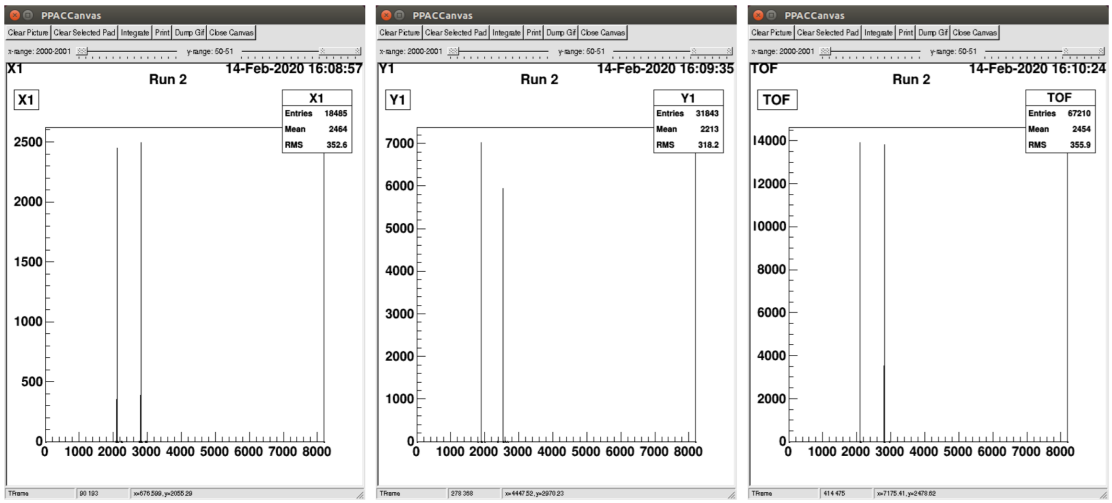

Gating on X1 (channels 2000-4000)

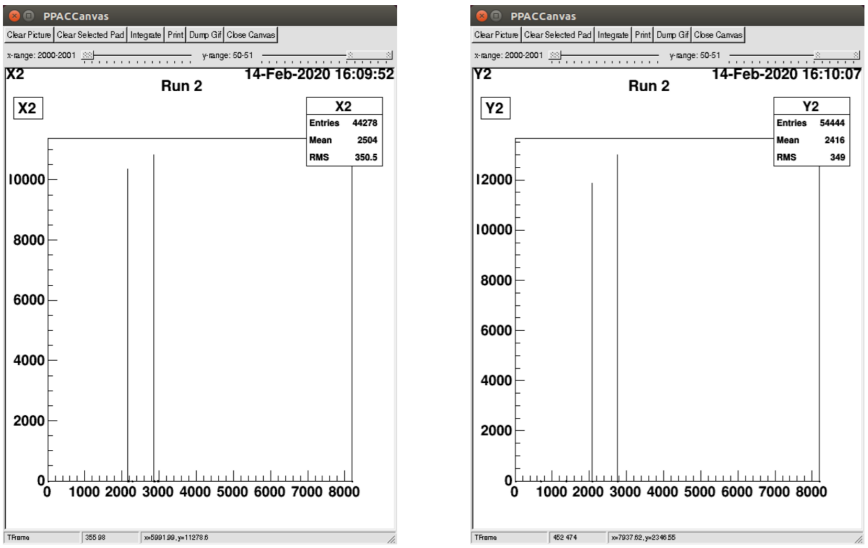

Figure A2: Histogram results with gates on x axis channels of the detector closest to source

Gating on TOF (channels 500-2000)

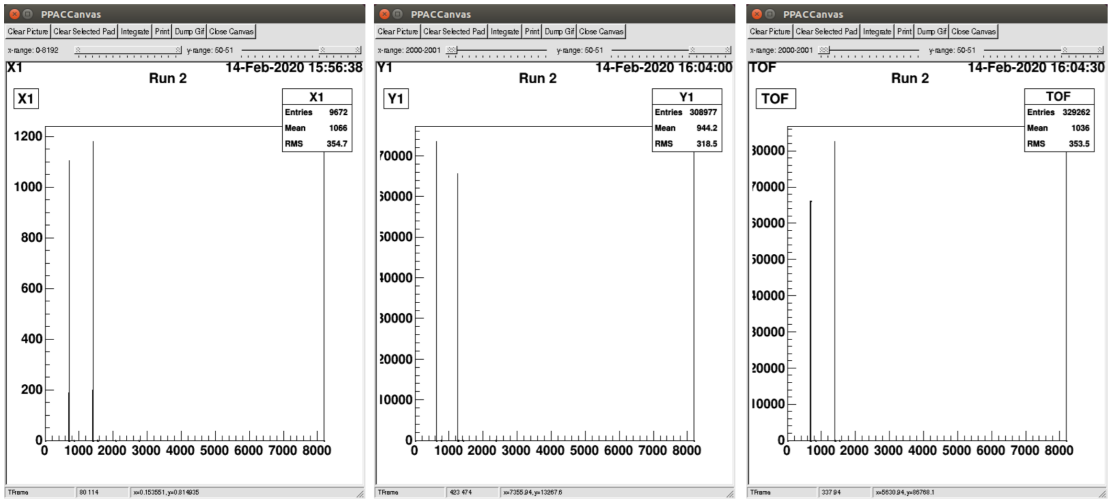

Gating on TOF (channels 500-2000)

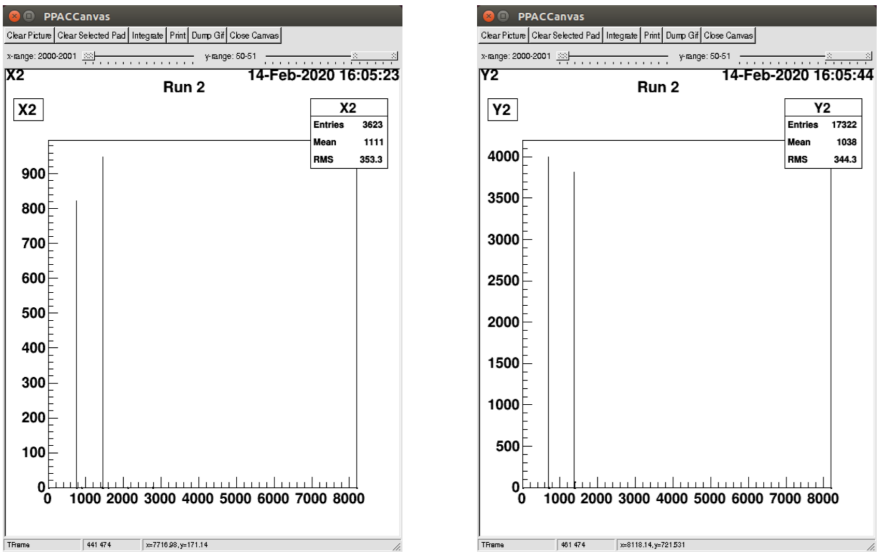

Figure A3: Histogram results with gates on time of flight channels

Table A1: PPAC Calibration Test

X1		Y1		X2		Y2	
Peak Channel	Peak Time (ns)	Peak Channel	Peak Time (ns)	Peak Channel	Peak Time (ns)	Peak Channel	Peak Time (ns)
680	80	601	80	738	80	653	80
1383	160	1232	160	1435	160	1357	160
2086	240	1866	240	2135	240	2066	240
2791	320	2502	320	2836	320	2776	320

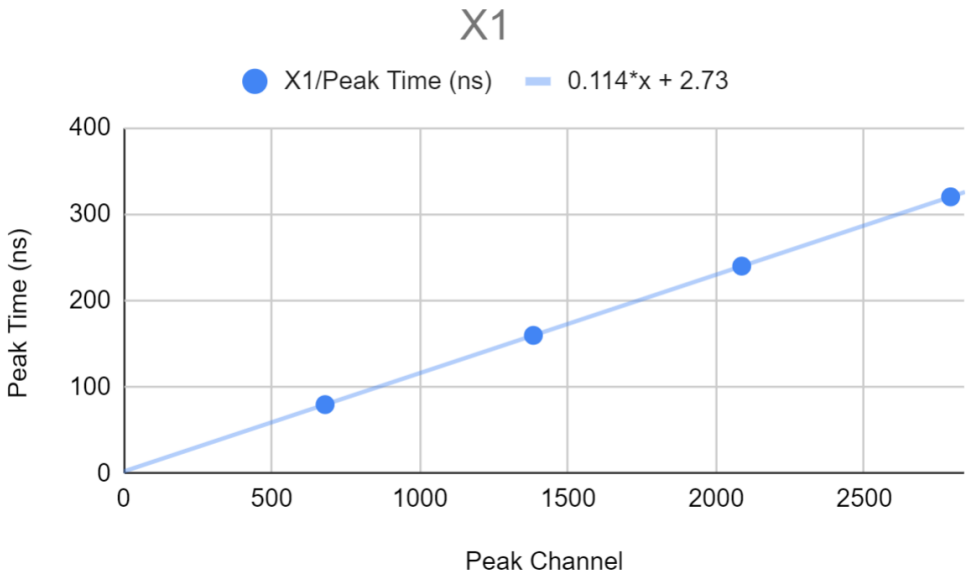

Figure A4: Calibration in x axis for detector closest to source

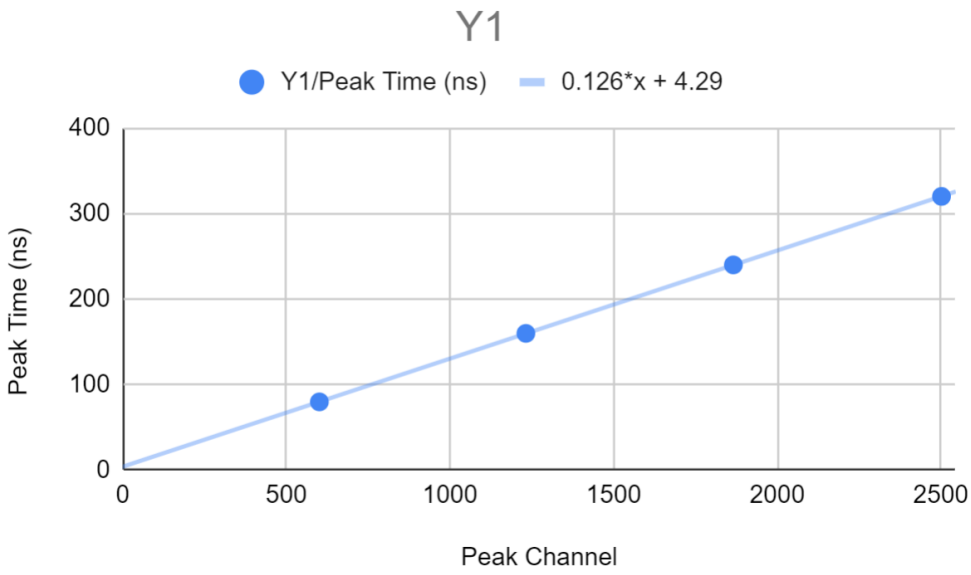

Figure A5: Calibration in y axis for detector closest to source

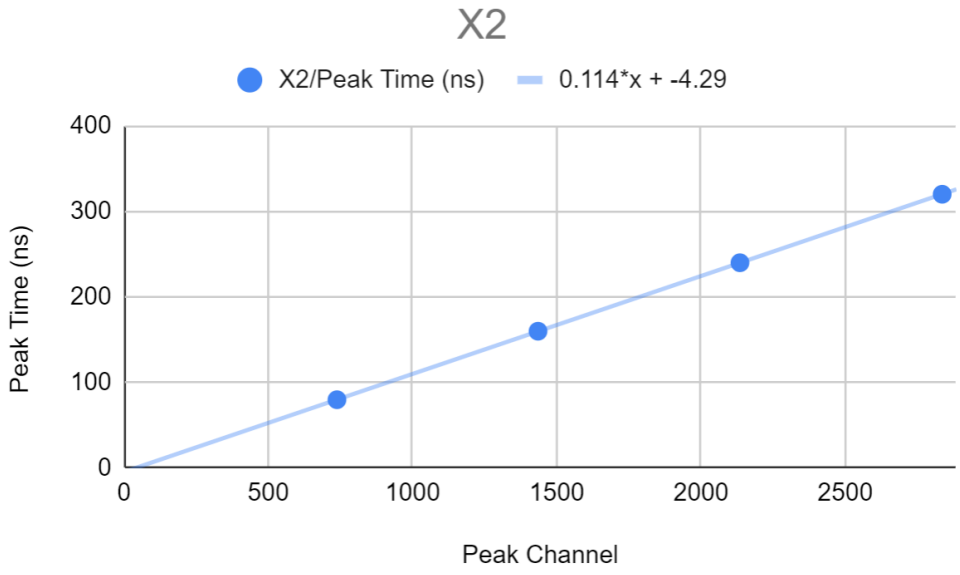

Figure A6: Calibration in x axis for detector farthest from source

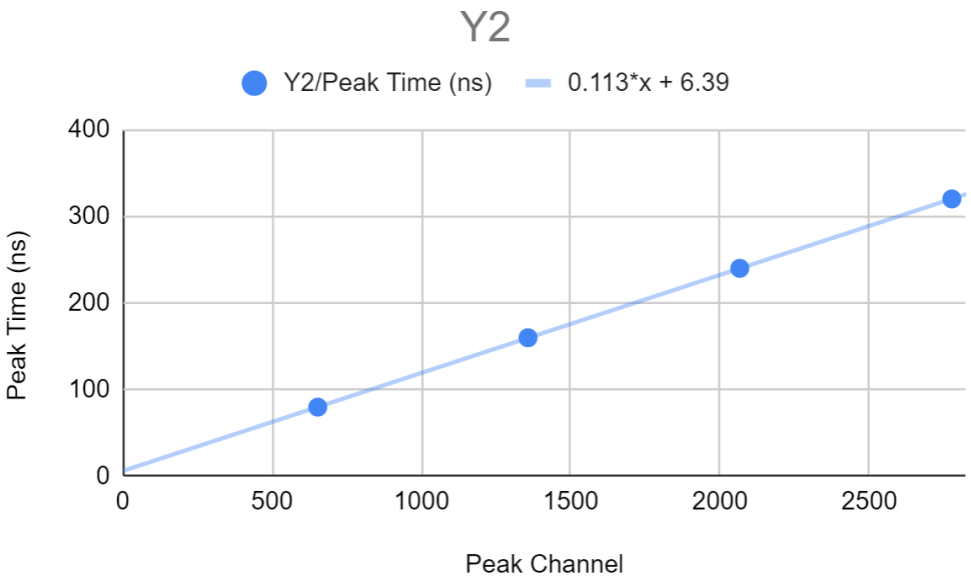

Figure A7: Calibration in y axis for detector farthest from source

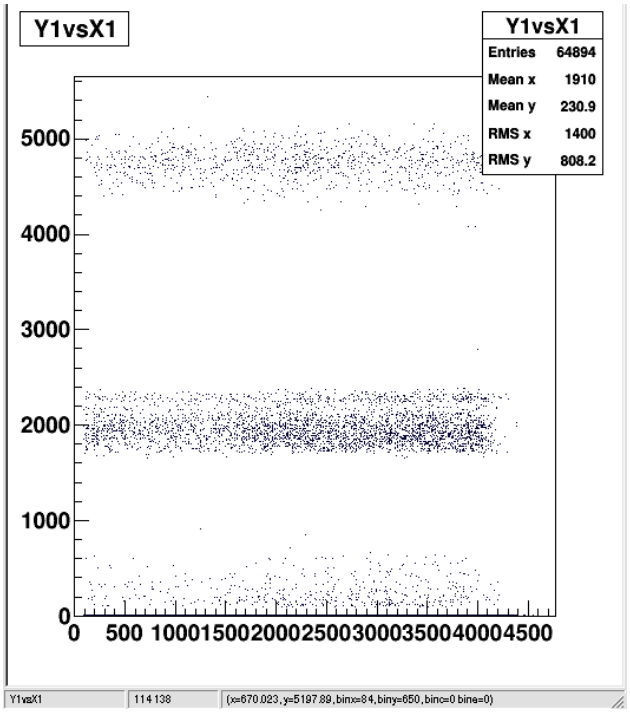

Figure A8: The first test performed using the alpha source. Notice the various bands of detection, which are created by having lower thresholds to detect a signal

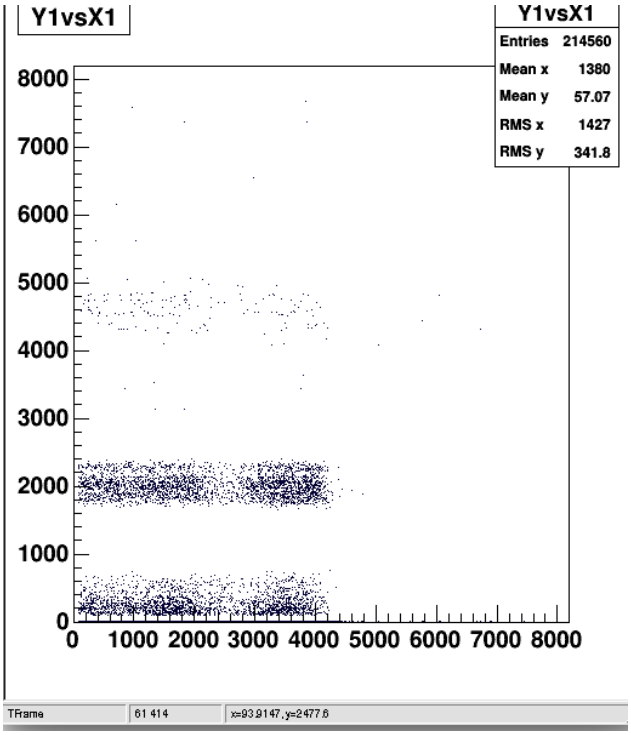

Figure A9: Another test, with pronounced lower bands due to reflections being detected

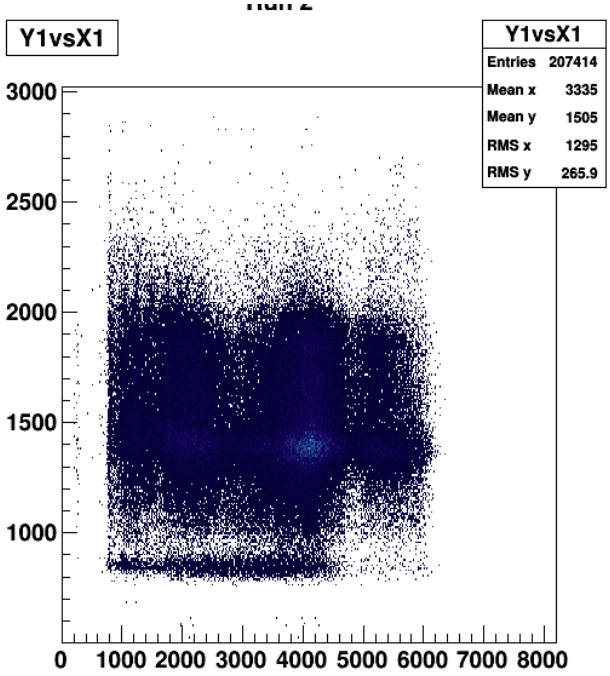

Figure A10: The first test that resulted in more conclusive detections

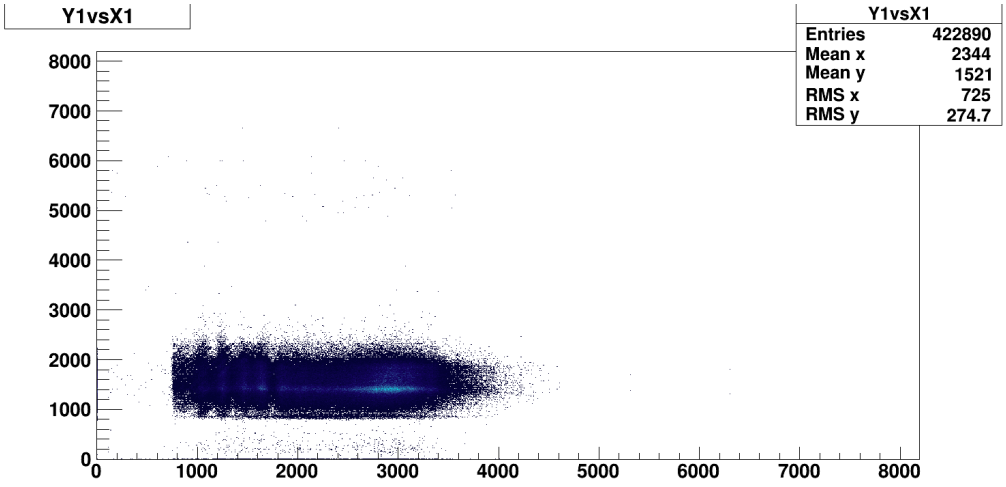

Figure A11: The source was moved from the left end of the detector towards the center slowly, allowing 30 seconds at each inch

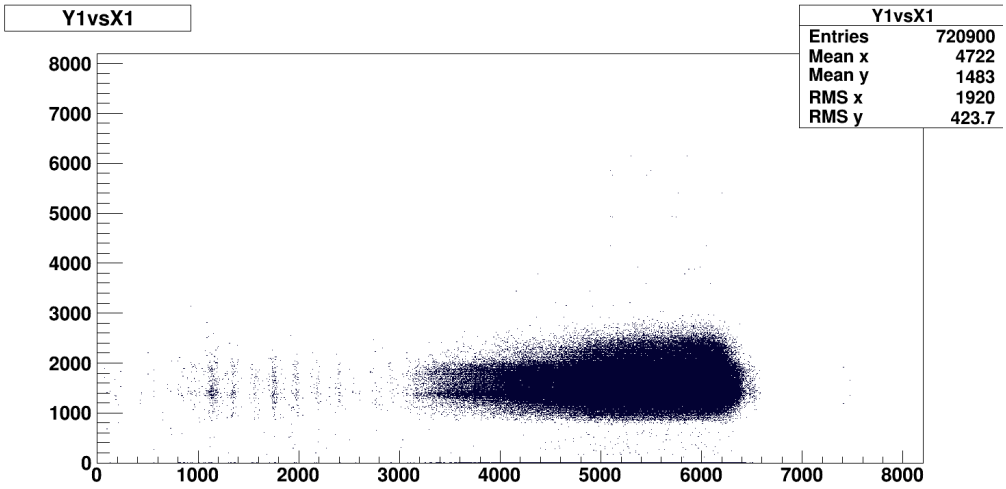

Figure A12: The source was moved from the right end of the detector towards the center slowly, allowing 30 seconds at each inch